AGU100 ADVANCING EARTH AND SPACE SCIENCE

Geophysical Research Letters

RESEARCH LETTER
10.1029/2018GL080013

Special Section:
The Three Major Hurricanes of 2017: Harvey, Irma and Maria

Near-Surface Maximum Winds During the Landfall of Hurricane Harvey

A. Addison Alford[1], Michael I. Biggerstaff[1,2,3], Gordon D. Carrie[1], John L. Schroeder[4,5], Brian D. Hirth[5], and Sean M. Waugh[6]

[1]School of Meteorology, University of Oklahoma, Norman, OK, USA, [2]Cooperative Institute for Mesoscale Meteorological Studies, University of Oklahoma, Norman, OK, USA, [3]Advanced Radar Research Center, University of Oklahoma, Norman, OK, USA, [4]Atmospheric Science Group, Texas Tech University, Lubbock, TX, USA, [5]National Wind Institute, Texas Tech University, Lubbock, TX, USA, [6]National Severe Storms Laboratory, Norman, OK, USA

Abstract A mobile Shared Mobile Atmospheric Research and Teaching (SMART) radar was deployed in Hurricane Harvey and coordinated with the Corpus Christi, TX, WSR-88D radar to retrieve airflow during landfall. Aerodynamic surface roughness estimates and a logarithmic wind profile assumption were used to project the 500-m radar-derived maximum wind field to near the surface. The logarithmic wind assumption was justified using radiosonde soundings taken within the storm, while the radar wind estimates were validated against an array of StickNets. For the data examined here, the radar projections had root-mean-squared error of 3.9 m/s and a high bias of 2.3 m/s. Mesovorticies in Harvey's eyewall produced the strongest radar-observed winds. Given the wind analysis, Harvey was, at most, a Category 3 hurricane (50–58 m/s sustained winds) at landfall. This study demonstrates the utility of integrated remote and in situ observations in deriving spatiotemporal maps of wind maxima during hurricane landfalls.

Plain Language Summary Measurements of extreme winds during hurricane landfall are difficult to obtain due to sparsely populated observing systems that cannot capture the complete distribution of the wind field. The wind fields are needed to refine building codes in hurricane prone areas and to delineate damage caused by wind versus water during poststorm assessment, particularly for insured losses. By using three-dimensional winds retrieved from two ground-based Doppler radars, the maximum wind distribution of Hurricane Harvey was analyzed. The radar winds were projected to the surface and validated against a network of anemometers, yielding close agreement. The analysis showed that Harvey was, at most, a Category 3 (sustained winds between 50 and 58 m/s) strength storm at landfall. Additionally, perturbations in the eyewall similar to the parent circulation of tornadic storms led to the strongest flow observed near the surface.

Key Points:
- Dual-Doppler wind retrievals show that Harvey was, at most, a Category 3 hurricane at landfall
- Mesovortices in the inner eyewall of Hurricane Harvey produced the strongest flow observed in the storm
- Mobile Doppler radar and in situ surface and upper air networks can improve estimates of near-surface winds during hurricane landfall

Supporting Information:
- Supporting Information S1

Correspondence to:
M. I. Biggerstaff,
drdoppler@ou.edu

Citation:
Alford, A. A., Biggerstaff, M. I., Carrie, G. D., Schroeder, J. L., Hirth, B. D., & Waugh, S. M. (2019). Near-surface maximum winds during the landfall of Hurricane Harvey. *Geophysical Research Letters*, *46*, 973–982. https://doi.org/10.1029/2018GL080013

Received 11 AUG 2018
Accepted 26 NOV 2018
Accepted article online 28 NOV 2018
Published online 16 JAN 2019

1. Introduction

Landfalling tropical cyclones (TCs) can devastate coastal communities via wind and water damage (Rappaport, 2014). Storm surge and inland flooding historically have been the primary cause of TC-related deaths in the United States, while damage to built structures by extreme winds has created property losses that exceed $10B (Huang et al., 2001; Klotzbach et al., 2018). In the past, the distribution of near-surface winds during TC landfall has been documented through surface measurements (Krupar et al., 2016; Powell et al., 1996; Powell & Houston, 1996, 1998) and dropsondes from aircraft (e.g., Rogers et al., 2017; Stern et al., 2016). Above the ground, psuedo-dual-Doppler and dual-Doppler wind retrievals from aircraft (Houze et al., 1992; Marks & Houze, 1987; Reasor et al., 2000) and single- and dual-Doppler analysis from surface-based fixed (Crum & Alberty, 1993) and mobile (Wakimoto & Srivastava, 2017) Doppler radars have documented the winds within TCs as well as boundary layer structure and evolution over land and coastal waters (Hirth et al., 2012; Knupp et al., 2006; Kosiba et al., 2013; Lorsolo et al., 2008).

Unlike sparse in situ surface observing platforms like the Automated Surface Observing Systems (Powell, 1993), dual-Doppler radar-based wind retrievals provide nearly continuous spatial distribution of winds over mesoscale areas (cf., Fernandez-Caban et al., 2018), while single-Doppler retrievals can discern low wavenumber components of the flow (Lee et al., 1999; Lee & Marks, 2000). Although surface friction over land decelerates TC airflow as the near-gradient wind balance is disrupted (Smith & Montgomery, 2014), the

primary vortex, mesogamma, and convective scale anomalies in the flow may still exhibit significant magnitudes (Black et al., 1999). Kilometer and subkilometer-scale features can also enhance the local wind field, magnifying the primary flow and lead to significant property damage (Powell & Houston, 1996; Wurman & Kosiba, 2018).

Since radars cannot measure winds near the surface for more than a few kilometers due to the Earth's curvature, relating damage at the surface to the retrieved winds aloft has generally been limited to correlating damage swaths on the ground with tracks of observed flow aloft, particularly for tornadic storms (e.g., Burgess et al., 2002; Wakimoto et al., 2003). To better understand the impact of long duration wind events like TCs on buildings, quantitative estimates of the near-surface winds (defined as 1-min average wind speed at 10-m altitude) are required (Knight & Khalid, 2015; Sparks et al., 1994). Moreover, time series of near surface winds over a continuous, broad area can help mitigate unnecessary litigation resulting from insured losses in areas affected by both extreme winds and floods or storm surge (Baradaranshoraka et al., 2017). Maps of the maximum near-surface wind and the time it occurred relative to water incursions would aid in targeting the most impacted areas for poststorm surveys and aid in understanding the scale of similarly caused losses.

In their study of Hurricane Rita (2005), Kosiba et al. (2013) demonstrated the utility of projecting the *radial* Doppler radar-observed wind above 100m to a 10-m estimated wind speed and validated the radial component projection using two in situ measurements. Attenuation of the X-band radar pulse limited the range of their analysis. To date, maps of spatially contiguous estimated maximum near-surface winds over an area of ~10^4 km^2 using the total wind vector from dual-Doppler analyses have not been provided.

In this study, data from fixed and mobile Doppler radars are combined to produce wind retrievals during the landfall of Hurricane Harvey (2017). Hurricane Harvey produced extreme winds in the Rockport and Port Aransas, TX, region and extensive flooding in eastern Texas and western Louisiana (Blake & Zelinsky, 2018). The radar-derived horizontal flow at 500-m altitude was projected to near the surface using a simple logarithmic profile with an aerodynamic surface roughness estimate at each grid point in the analysis. A logarithmic wind profile assumption is an appropriate method to reduce elevated wind measurements to near the surface when the measurements are at or below the altitude of the hurricane wind maxima (Franklin et al., 2003). The method used here was tested against radiosonde wind profiles, and the radar estimated winds were validated against in situ measurements from a network of StickNets (Weiss & Schroeder, 2008). The estimated winds agreed well with the in situ observations. Additionally, several of the peak maximum surface winds coincided with paths of mesovorticies that circulated around the eyewall of the hurricane. This is the first time that spatially contiguous maps covering ~10^4 km^2 area of the maximum near-surface winds during the landfall of a major hurricane have been presented.

2. Data and Analysis Methods

2.1. Radar

For this study, data from the Corpus Christi, TX National Weather Service (NWS) WSR-88D (KCRP) located at 27.7840°N, 97.5113°W was combined with the SR2 C-band Shared Mobile Atmospheric Research and Teaching (SMART) radar (Biggerstaff et al., 2005). SR2, located at 28.1480°N, 97.4101°W, collected volumetric data between 2058 UTC on 25 August 2017 and 1630 UTC on 26 August. The locations of instruments used in this study are shown in Figure SF1. SR2 operated nearly continuously with the exception of two periods, 2305–2350 UTC on 25 August and 0140–0310 UTC on 26 August, during which the radar suffered antenna drive failures. The 42-km baseline between the two radars was oriented quasi-parallel to the Texas coastline. This arrangement afforded wind retrieval areas over land to the northwest of the baseline and over the immediate coastal areas and into the Gulf of Mexico southeast of the baseline. Only the southeastern area was examined for this study. While both radars are dual-polarimetric, only the radial velocity and radar reflectivity were used.

The velocity data were dealiased with the Python ARM Radar Toolkit (Helmus & Collis, 2016) and then further quality controlled using Solo3 (Oye et al., 1995). Following Betten et al. (2018), the radial velocity and reflectivity were interpolated to a Cartesian grid via a natural neighbor interpolation scheme (Sibson, 1981). The analysis domain origin is located at KCRP with a horizontal and vertical grid spacing of 1.0 km. Horizontally, the analysis grid extended from 0 to 130 km in the zonal direction and −60 to 70 km

in the meridional direction. Vertically, the grid started at 0.5 km and extended to 10.5 km. Dual-Doppler wind syntheses were performed approximately every 5 min using the variational retrieval method of Potvin et al. (2012).

A map of the maximum wind speed at 500 m for each grid point for two periods, one before the official landfall (about 0300 UTC on 26 August) and the other after, were constructed along with the time the maximum occurred for each grid point. The 500-m altitude was chosen to minimize the distance required to project winds to the surface while maintaining a broad region of coverage. Following Hirth et al. (2012), the aerodynamic roughness length Z_0 (in m) was derived from Office for Coastal Management land cover maps (National Oceanic and Atmospheric Administration, 2018) to project the 500-m winds to the near surface. Using a simple logarithmic profile (equation (1)), the projected wind speed *Utower* (in m/s) at height *Ztower* was calculated from the radar wind speed *U500* (in m/s) at 500 m (*Z500*).

$$\mathrm{Utower} = \mathrm{U500}\,\frac{\ln\left(\frac{\mathrm{Ztower}}{\mathrm{Zo}}\right)}{\ln\left(\frac{\mathrm{Z500}}{\mathrm{Zo}}\right)} \tag{1}$$

While there are uncertainties in the representativeness of a logarithmic wind profile within TC boundary layers (Smith & Montgomery, 2014), especially as the internal boundary layer evolves (Hirth et al., 2012), a similar logarithmic profile was applied by Kosiba et al. (2013) to estimate near-surface winds during the landfall of Hurricane Rita. To appropriately filter the 30-m resolution surface roughness data to the scale of the radar-retrieved wind analysis, the closest 10 surface roughness points at each StickNet site were averaged to obtain the Z_0 value used in the projection. Winds were projected to both 10- and 2.25-m heights. Ten meters is the standard height used for NWS surface wind measurements, while the StickNet anemometers, used for validation, were at a height of 2.25 m.

2.2. StickNets

Texas Tech University deployed a fleet of 14 StickNet portable observing weather platforms in the landfall region of Hurricane Harvey. Each platform utilized an RM Young 05103 wind monitor operating at a sampling frequency of 10 Hz and at a measurement height of 2.25 m above ground level. Each wind speed time history used herein underwent manual quality control where suspect or erroneous data were removed. Ten and 30-s wind speed averages were then constructed centered on the time of maximum observed dual-Doppler wind speed at the grid point closest to the StickNet deployment location (Table S1). Site photos were taken both at the time of deployment and retrieval of the instruments to document the surrounding surface roughness, including signs of localized flooding or damage during the event. The inner core of Harvey passed over the array of StickNets, seven of which were in the dual-Doppler retrieval region (Figure S1) and were used to validate the projection of the radar winds to the surface.

Using the advective time-to-space relationship for airflow, the spatial scales of the radar analyses correspond to about a 30-s average of winds measured at a point for the observed wind speeds. Hence, the in situ winds were averaged over a 30-s period centered on the time of the radar recorded maximum wind at the point over each StickNet location.

2.3. Soundings

To evaluate the logarithmic wind profile assumption, data were used from two radiosonde soundings (Figure S2) launched from a mobile mesonet operated by the National Severe Storms Laboratory. The first sounding was launched at 1954 UTC on 25 August 2017 at 28.2640°N, 97.3018°W and the second at 0136 UTC on 26 August 2017 at 28.1597°N, 97.4009°W. The soundings employed a Vaisala RS41-SGP radiosonde. Technical specifications for the RS41-SGP include a temperature uncertainty of 0.3 °C, over a −95 °C to +60 °C range, a 0.5-s temperature response time, humidity observations accurate to within 4%, and an onboard pressure sensor with accuracy of 1 hPa.

The RS41-SGP derives wind speed and direction using a proprietary smoothing algorithm applied to the change in location determined from a GPS receiver. The derived winds have a stated accuracy of 0.15 m/s and 2°, respectively. Given the unknown nature of the smoothing algorithm, an unfiltered wind profile was derived for this study using recorded GPS locations. To avoid regions of downdraft, where momentum mixing would affect the wind speed, data were removed when the ascent rate of the balloon was less than 2 m/s.

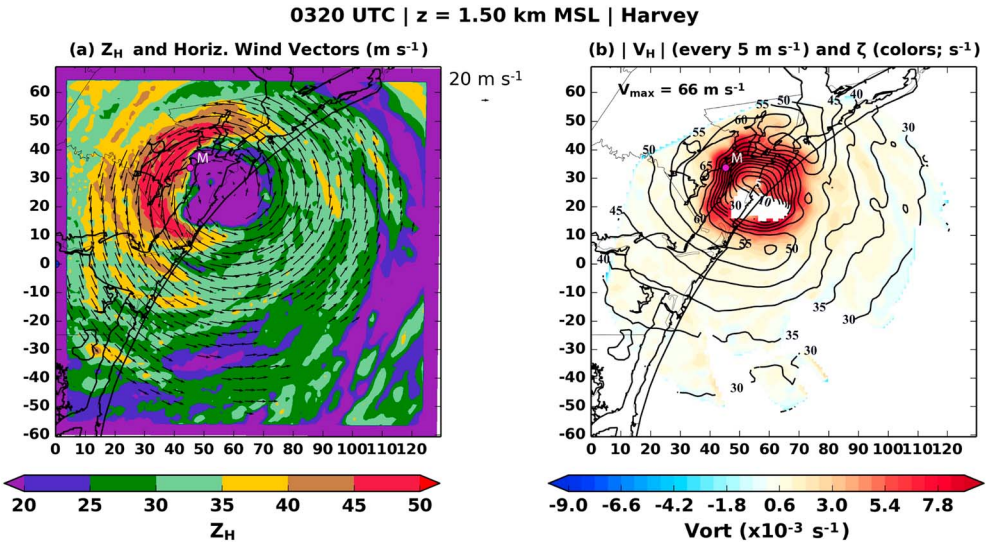

Figure 1. Dual-Doppler analysis at 0320 UTC during Hurricane Harvey's landfall. (a) The color-filled contours show radar reflectivity (Z_H, in dBZ) every 5 dB. The ground-relative wind vectors indicate the magnitude and direction of the horizontal wind with a reference vector shown in the top right part of the figure. (b) The black contours indicate the magnitude of the horizontal wind every 5 m/s. The color-filled contours are vertical vorticity X10^{-3}/s. The *M* indicated the location of the mesovortex discussed in the text.

3. Wind Retrievals at 500-m Altitude

3.1. Single Wind Retrieval

At landfall, Hurricane Harvey was estimated to be a category four storm (58–70 m/s) by the National Hurricane Center (Blake & Zelinsky, 2018) with a maximum sustained wind of approximately 59 m/s. As shown in the 0320 UTC dual-Doppler wind field analysis, the area of extreme winds in Harvey was rather compact (Figure 1). At 500-m, dual-Doppler winds approached 70 m/s in the eyewall. While this observation appears extreme, examination of radial velocity in the lowest elevation angle sweeps from SR2 and KCRP revealed Doppler velocities exceeding 70 m/s at several locations during landfall (not shown). The strong winds (>60 m/s) in the western eyewall were confined to a narrow swath slightly upstream (clockwise) from a mesovortex (Figure 1b) that was similarly noted in Fernandez-Caban et al. (2018). Thus, the mesovortex winds do not necessarily represent the broader-scale mean wind. Due to the presence of this and other mesovortices circulating along the inner eyewall, the eyewall resembled a wavenumber four pattern in both reflectivity and vertical vorticity.

At a range of approximately 40 km from the center of circulation, the horizontal wind magnitude decreased to about 50 m/s. At approximately 50-km range, the horizontal wind decreased to about 40 m/s. Thus, at the time under consideration, the most extreme winds were largely confined to within 30 km of the center of circulation.

3.2. Distribution of Maximum Wind at 500-m Altitude

To assess the distribution of the 500-m maximum wind, time series of analyses were conducted with the maximum wind speed and time of occurrence recorded at each data point. Two periods are included, one before official landfall (2058 UTC on 25 August to 0139 UTC on 26 August; Figures 2a and 2b) and one during landfall (0314 UTC—0556 UTC on 26 August; Figures 2c and 2d). The SR2 radar was inoperable between 0140 UTC and 0310 UTC.

The eyewall path can be clearly distinguished in the maximum wind field prior to landfall (Figure 2a). Wind speeds near 70 m/s characterized the western portion of the eyewall. Southwest of the eyewall path, the maximum 500-m wind was generally less than 50 m/s. Similar to the analysis at 0320 UTC, the gradient in the maximum horizontal wind radially outward from the eyewall was readily discernable.

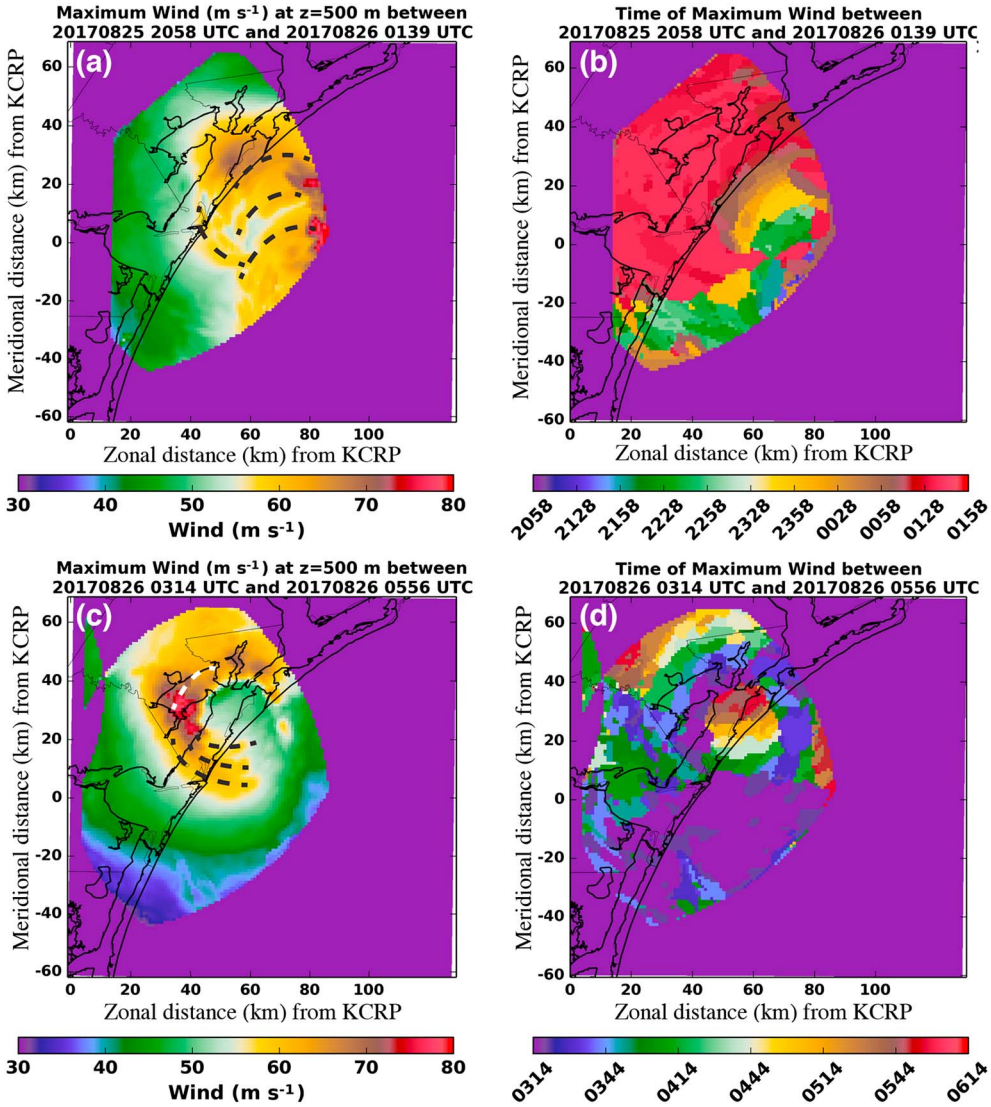

Figure 2. In (a) the maximum horizontal wind that occurred at each grid point between 2058 and 0139 UTC is shown for the 500-m altitude analysis. The abscissa is east-west distance from KCRP, while the ordinate is the north-south distance from KCRP. (b) The time at which the maximum wind occurred at each grid point. Panels (c) and (d) are similar but for the 0314–0556 UTC period. The dashed lines in (a) and (c) denote mesovortex tracks clearly distinguishable in the individual wind retrieval analyses.

Distinct, arc-shaped swaths of localized wind maxima were also found as Harvey moved toward shore, including one late in the period that was oriented northwest-to-southeast (centered at $x = 50$, $y = -10$ km in Figure 2a). Further inspection revealed that these swaths in the maximum wind field were the result of individual mesovortices in Harvey's eyewall. On the scale of the wind retrievals, the mesovortices created an additional 5–10 m/s of wind speed relative to the airflow at surrounding points. The temporal evolution of the maximum wind prior to landfall (Figure 2b) indicates that these local structures revolved cyclonically in time around the inner eyewall and were associated with the strongest observed winds.

During landfall (0314–0556 UTC; Figures 2c and 2d), the maximum wind field exhibited similar characteristics. The strongest winds were still confined to within 30 km of the center of circulation and sharply decreased radially outward. Moreover, the maximum winds at 500 m over land appeared to be just as strong as the winds prior to landfall offshore. Subsections of the eyewall had 500-m maximum winds between 75 and 80 m/s during 0330 to 0345 UTC over Copano Bay and Rockport, TX ($x = 35$, $y = -35$ in Figure 2c), where significant wind damage occurred.

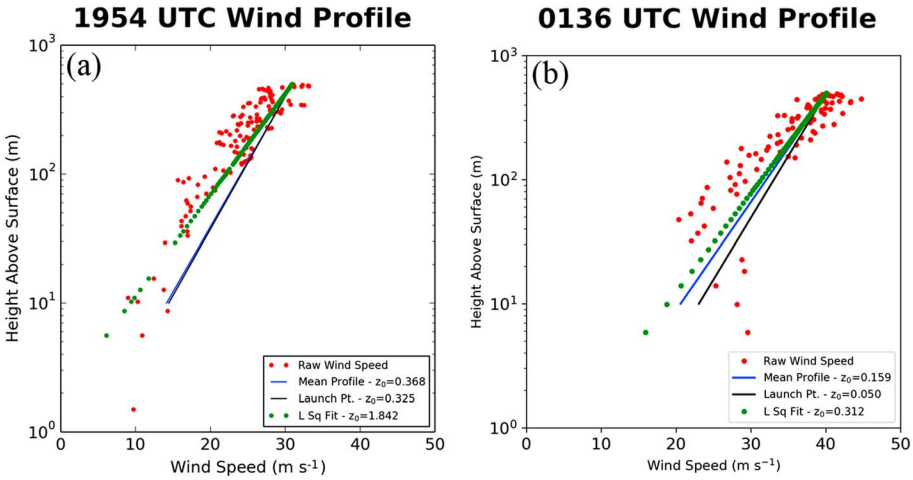

Figure 3. Unfiltered winds, for balloon ascent rates greater than 2 m/s, in the lowest 500 m of the radiosonde soundings taken at (a) 1954 UTC on 25 August 2017 and (b) 0136 UTC on 26 August 2017. The blue (black) lines show the projected wind profile for the 10-point average (along balloon path average) surface roughness. The green line is the least squares best fit to the unfiltered winds.

The mesovortices likely responsible for the local enhancements in the maximum wind are thought to be associated with vortex Rossby waves (VRWs; Montgomery & Kallenbach, 1997) due to their propagation against the mean flow (Gao & Zhu, 2016; Wingo & Knupp, 2016; Wurman & Kosiba, 2018). VRWs are hypothesized to promote the redistribution of momentum in TC eyewalls (Gao & Zhu, 2016; Montgomery & Kallenbach, 1997; Wang, 2002a, 2002b). Alford and Biggerstaff (2017) found a similar mesovortex/VRW structure in the decaying eyewall of Hurricane Hermine (2016) during landfall that also locally intensified wind speed as the broader-scale primary circulation decreased in strength. While these observations are at 500-m altitude, the wind gusts observed by Fernandez-Caban et al. (2018) at the surface near one of these mesovortices imply that the mesovortices produce enhanced surface wind perturbations as well. Future studies will examine the Harvey data set in more detail to elucidate the role of VRWs in the generation of mesovortices and inner core rainbands.

4. Wind Estimates Near the Surface

Diagnosis of maximum winds in landfalling TCs generally relies on overocean dropsonde observations of the near-surface wind field and projections of in situ measurements from airborne platforms, such as the National Oceanic and Atmospheric Administration P-3, to the near surface (Franklin et al., 2003). Here we make use of the surface roughness lengths derived from land use maps obtained from the Office for Coastal Management (Figure S3) to project the 500-m maximum winds to 10 m, which corresponds to the height of standard surface wind measurements conducted by the National Weather Service, and 2.25 m, which corresponds to the height of the anemometers on the StickNets.

4.1. Validation of the Wind Projections

To evaluate the logarithmic wind profile assumption, unfiltered wind speed data from two mobile surface-based soundings released in an outer rainband at 1954 UTC and within the inner core at 0136 UTC were examined (Figure 3). Both profiles indicate that the 500-m altitude was below the level of maximum wind, which would suggest that a logarithmic wind profile is appropriate (Franklin et al., 2003). Indeed, the unfiltered winds fit a logarithmic wind speed profile reasonably well. Using an average of the surface roughness around the launch site, extrapolations of the sounding-observed 500-m wind to 10 m led to differences of about 4 m/s (~25%) compared to the sounding-observed 10-m wind. Using an average of surface roughness along the path of the balloon as it rose from the surface to 500 m improved the estimated wind profile fit for the later, inner core, sounding but did not appreciably change the earlier sounding estimated wind speed profile. Indeed, the surface roughness associated with the least squares fit of the unfiltered wind for the later sounding was close to the average surface roughness following the balloon location. In contrast, the least

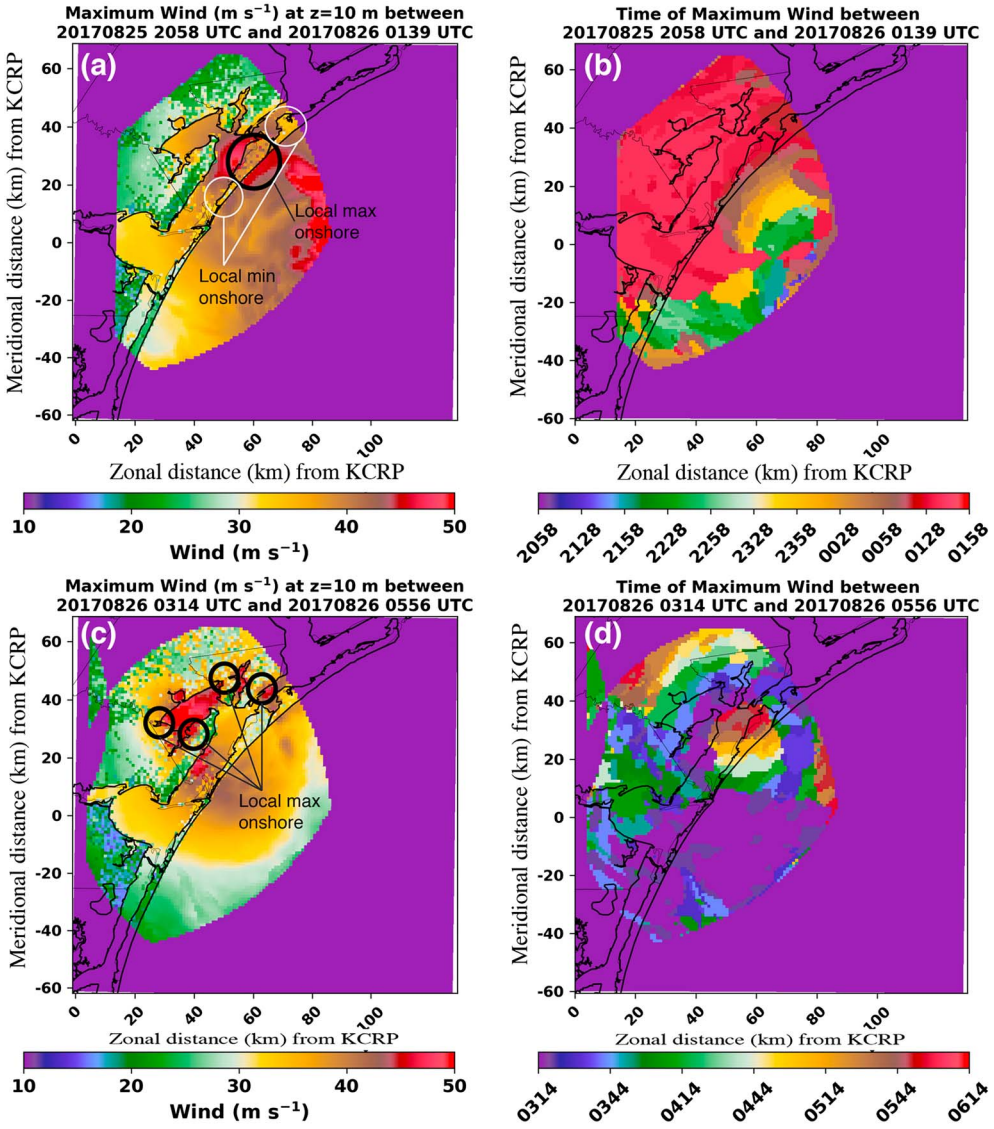

Figure 4. (a) The maximum 10-m wind experienced between 2058 and 0139 UTC on 25–26 August. (b) The time at which the maximum wind in (a) occurred. (c) The maximum 10-m wind experienced between 0314 and 0556 UTC on 26 August. (d) The time at which the maximum 10 m was observed in (c). For (a) and (c), the 10-m wind was projected from the 500-m wind. The circles in (a) and (c) denote regions of maxima and local minima in winds as discussed in the text.

squares fit surface roughness for the earlier sounding taken in an outer rainband was significantly higher than the nearby average, the average following the balloon, or the single surface roughness value at the launch site.

Further validation of the results from applying the logarithmic profile was accomplished by projecting the radar maximum winds to the seven StickNet locations in the radar domain (Table S1). The 30-s average winds from the StickNets were compared against the radar projections using (1) with the surface roughness estimate taken from the average of the closest 10 points to each StickNet location. Comparing the radar projections to the in situ measurements led to a root-mean-squared error of 3.9 m/s and an average radar high bias of 2.3 m/s, which is close to the sounding data projection.

While the number of validation points is low, the greatest error occurred in low surface roughness locations. These locations were very close to the shoreline. Hence, many of the closest surface roughness points were over water. Using dual-Doppler analyses, Hirth et al. (2012) showed that there is a rapid decrease in the boundary layer wind speed as air crosses the ocean-land interface. Thus, the radar-estimated maximum

winds near the coastline (within 300–500 m) may be overestimated by ~20%. Elsewhere, the errors were about 10% of the in situ measured wind speed at 2.25 m.

4.2. Spatially Continuous Projections

The 500-m maximum wind fields between 2058–0139 UTC and 0314–0556 UTC were projected to 10 m using the same procedure as for the validation (Figure 4). (A combined wind map is shown in Figure S3. The surface roughness values used in the projection are shown in Figure S4). Since the aerodynamic surface roughness is assumed to be constant over the open water, the near-surface projection does not consider changes in sea surface roughness that were likely present (Powell et al., 2003). Otherwise, the impact of surface roughness variability on the near surface wind estimates is apparent (Figure 4). Airflow over open water was significantly stronger than along the coast and inland. Maxima of 45–50 m/s in the projected wind can be seen offshore both in the Gulf of Mexico and in Aransas Bay in association with the path of the eyewall and embedded mesovortices. Indeed, a large swath of strong flow (greater than 45 m/s) crossed the unpopulated National Wildlife Preserve on Matagorda Island (area enclosed in black circle in Figure 4a) between 0100 and 0130 UTC on 26 August (Figure 4b). Examining individual analyses (not shown) revealed that the strongest wind was associated with the path of a mesovortex. Elsewhere, winds over the barrier islands of the Texas coast were 30–35 m/s as the northwestern portion of the eyewall moved on shore near 0130 UTC.

During the latter part of landfall (Figures 4c and 4d) the strongest winds (about 50 m/s) were found in Copano Bay ($x = 40$ km, $y = -35$ km in Figure 4c). Several locations along the shore of Copano Bay experienced winds in excess of 45 m/s, including the towns of Bayside and Holiday Beach (western circles in Figure 4c). Another local maximum, around the same timeframe, was found between Aransas Pass and Rockport, TX, in association with tracks of mesovortices (Figure 2c). Around 0600 UTC, another swath of winds in excess of 45 m/s occurred in an unpopulated area (easternmost black circle in Figure 4c). While the presence of the strongest projected winds was largely confined to near the coast where the surface roughness might be underestimated, these maxima do extend 1–5 km inland. In the United States, a 1-min average wind speed at 10-m height is used to classify hurricane strength. The spatial extent of the maximum winds shown here suggests that Harvey was, at best, a Category 3 (50–58 m/s) hurricane at landfall. It is important to note, however, that the SR2 radar was off-line during a portion of the landfall and the wind record here is incomplete. Nevertheless, the radial velocity data from KCRP did not indicate stronger winds were present during the time SR2 was unavailable.

5. Conclusions

In this study, data from a mobile C-band SMART radar were combined with the Corpus Christi, TX, WSR-88D radar to examine the maximum winds that occurred before and after the landfall of Hurricane Harvey. Individual dual-Doppler wind retrievals, conducted about every 5 min, were used to construct a map of the maximum wind magnitude and time of occurrence at 500 m for every grid point in the radar domain. Aerodynamic surface roughness estimates were applied within a logarithmic wind profile to extrapolate the 500-m radar maximum winds to wind speeds near the surface.

The technique was evaluated using soundings from a mobile platform and further validated against a small network of in situ anemometers. It was found that the projected radar wind speeds were within 10–20% of the in situ measurements when examining 30-s anemometer averages, which is consistent with the time-space conversion for the observed flow and the ~1-km spacing of the radar data. The errors were largest for small surface roughness estimates, which likely reflect the inclusion of open-water values in estimating the average roughness for nearshore locations.

The projected wind speeds indicate that Hurricane Harvey was, at most, a Category 3 storm at the time of landfall, with a few locations around Copano Bay and near Rockport, TX, having large enough regions of winds in excess of 45 m/s to have produced a 1-min average wind of Category 3 strength. More importantly, the strongest winds found in the analysis were associated with tracks of individual mesovortices that circulated cyclonically around the eyewall of Hurricane Harvey. It is believed that these mesovortices were associated with VRWs generated by asymmetries in the eyewall during landfall. At the scale of the radar wind retrievals, the mesovortices enhanced the flow by 5–10 m/s relative to surrounding areas. Strong vertical drafts in mesovorticies (Wingo & Knupp, 2016) may mix high momentum parcels toward the surface at

scales that were not examined here. Moreover, the logarithmic wind profile used to project the radar winds to the near the surface may not be well suited to flow within and underneath mesovortices. Given observations of extreme gusts in such events (Black et al., 1999; Fernandez-Caban et al., 2018; Wurman & Kosiba, 2018), it is believed that the analysis presented here may underestimate, rather than an overestimate smaller scale wind maxima associated with mesovortices, or other wind gusts associated with a time scale of less than 30 s.

Regions of enhanced surface winds, especially in mesovorticies, demonstrate that the presence of local maxima are vital to understanding regions of maximum wind damage and the landfall structure of TCs. Spatially and temporally continuous observations from dual-Doppler analyses can capture these maxima, signifying that such data sets would be useful in hurricane wind engineering assessments. Indeed, a study in currently underway to relate damage to built structures to the dual-Doppler derived wind attributes presented here. Additionally, a time series of wind maxima associated with landfalling storms may help to better separate property losses from winds to those caused by surge and inland flooding. The dual-Doppler-derived wind fields can also be used to validate high-resolution numerical simulations of Harvey. Further characterization of the atmospheric boundary layer wind profile during hurricane landfall and a greater number of in situ measurements are needed to refine the wind projection method and yield more robust validation of radar estimated wind maxima at the surface.

Acknowledgments
Data collection for this study was supported by RAPID grant AGS-1759479 from the National Science Foundation and funds from the School of Meteorology at the University of Oklahoma. The first author was supported by NASA Headquarters under the NASA Earth and Space Science Fellowship Program grant 17-EARTH17R-72. The data used in the figures are available at Zenodo using doi: https://doi.org/10.5281/zenodo.1453446.

References

Alford, A. A., & Biggerstaff, M. I. (2017). Mesoscale processes observed in the inner cores of Hurricanes Hermine and Matthew. In *18th Cyclone Workshop*. Montreal, Canada: State University of New York at Albany.

Baradaranshoraka, M., Pinelli, J.-P., Gurley, K., Peng, X., & Zhao, M. (2017). Hurricane wind versus storm surge damage in the context of a risk prediction model. *Journal of Structural Engineering*, *143*(9), 1–10. https://doi.org/10.1061/(ASCE)ST.1943-541X.0001824

Betten, D. P., Biggerstaff, M. I., & Ziegler, C. L. (2018). Three-dimensional storm structure and low-level boundaries at different stages of cyclic mesocyclone evolution in a high-precipitation tornadic supercell. *Advances in Meteorology*, 1–24. https://doi.org/10.1155/2018/9432670

Biggerstaff, M. I., Wicker, L. J., Guynes, J., Ziegler, C., Straka, J. M., Rasmussen, E. N., et al. (2005). The shared mobile atmospheric research and teaching radar: A collaboration to enhance research and teaching. *Bulletin of the American Meteorological Society*, *86*(9), 1263–1274. https://doi.org/10.1175/BAMS-86-9-1263

Black, P. G., Buchan, S. J., & Cohen, R. L. (1999). The tropical cyclone eyewall mesovortex: A physical mechanism explaining extreme peak gust occurrence in TC Olivia, 4 April 1996 on Barrow Island, Australia. In *Offshore Technology Conference* (p. OTC 10792). Houston, TX.

Blake, E. S., & Zelinsky, D. A. (2018). National Hurricane Center Tropical Cyclone Report: Hurricane Harvey.

Burgess, D. W., Magsig, M. A., Wurman, J., Dowell, D. C., & Richardson, Y. (2002). Radar observations of the 3 May 1999 Oklahoma City tornado. *Weather and Forecasting*, *17*(3), 456–471. https://doi.org/10.1175/1520-0434(2002)017<0456:ROOTMO>2.0.CO;2

Crum, T. D., & Alberty, R. L. (1993). The WSR-88D and the WSR-88D operational support facility. *Bulletin of the American Meteorological Society*, *74*(9), 1669–1687. https://doi.org/10.1175/1520-0477(1993)074<1669:TWATWO>2.0.CO;2

Fernandez-Caban, P. L., Alford, A. A., Bell, M. J., Biggerstaff, M. I., Carrie, G. D., Hirth, B. D., et al. (2018). Observing Hurricane Harvey's eyewall at landfall. *Bulletin of the American Meteorological Society*. https://doi.org/10.1175/BAMS-D-17-0237.1

Franklin, J. L., Black, M. L., & Valde, K. (2003). GPS Dropwindsonde wind profiles in hurricanes and their operational implications. *Weather and Forecasting*, *18*(1), 32–44. https://doi.org/10.1175/1520-0434(2003)018<0032:GDWPIH>2.0.CO;2

Gao, C., & Zhu, P. (2016). Vortex Rossby wave propagation in baroclinic tropical cyclone-like vortices. *Geophysical Research Letters*, *43*, 12,578–12,589. https://doi.org/10.1002/2016GL071662

Helmus, J. J., & Collis, S. M. (2016). The Python ARM Radar Toolkit (Py-ART), a library for working with weather radar data in the Python programming language. *Journal of Open Research Software*, *4*(1), e25. https://doi.org/10.5334/jors.119

Hirth, B. D., Schroeder, J. L., Weiss, C. C., Smith, D. A., & Biggerstaff, M. I. (2012). Research radar analyses of the internal boundary layer over Cape Canaveral, Florida, during the landfall of Hurricane Frances (2004). *Weather and Forecasting*, *27*(6), 1349–1372. https://doi.org/10.1175/WAF-D-12-00014.1

Houze, R. A., Marks, F. D., & Black, R. A. (1992). Dual-aircraft investigation of the inner core of Hurricane Norbert. Part II: Mesoscale distribution of ice particles. *Journal of the Atmospheric Sciences*, *49*(11), 943–963. https://doi.org/10.1175/1520-0469(1992)049<0943:DAIOTI>2.0.CO;2

Huang, Z., Rosowsky, D. V., & Sparks, P. R. (2001). Hurricane simulation techniques for the evaluation of wind-speeds and expected insurance losses. *Journal of Wind Engineering and Industrial Aerodynamics*, *89*(7–8), 605–617. https://doi.org/10.1016/S0167-6105(01)00061-7

Klotzbach, P. J., Bowen, S. G., Pielke, R. Jr., & Bell, M. (2018). Continental U.S. hurricane landfall frequency and associated damage observations and future risks. *Bulletin of the American Meteorological Society*, *99*(7), 1359–1376. https://doi.org/10.1175/BAMS-D-17-0184.1

Knight, R. I., & Khalid, F. (2015). Evaluation of the potential of friction surface analysis in modelling hurricane wind damage in an urban environment. *Natural Hazards*, *76*(2), 891–911. https://doi.org/10.1007/s11069-014-1527-3

Knupp, K. R., Walters, J., & Biggerstaff, M. (2006). Doppler profiler and radar observations of boundary layer variability during the landfall of Tropical Storm Gabrielle. *Journal of the Atmospheric Sciences*, *63*(1), 234–251. https://doi.org/10.1175/JAS3608.1

Kosiba, K., Wurman, J., Masters, F. J., & Robinson, P. (2013). Mapping of near-surface winds in Hurricane Rita using fine scale radar, anemometer, and land-use data. *Monthly Weather Review*, *141*(12), 4337–4349. https://doi.org/10.1175/MWR-D-12-00350.1

Krupar, R. J., Schroeder, J. L., Smith, D. A., Kang, S.-L., & Lorsolo, S. (2016). A comparison of ASOS near-surface winds and WSR-88D-derived wind speed profiles measured in landfalling tropical cyclones. *Weather and Forecasting*, *31*(4), 1343–1361. https://doi.org/10.1175/WAF-D-15-0162.1

Lee, W.-C., Jou, B., Chang, P.-L., & Deng, S.-M. (1999). Tropical cyclone kinematic structure retrieved from single-Doppler radar observations. Part I: Interpretation of Doppler velocity patterns and the GBVTD technique. *Monthly Weather Review*, *127*(10), 2419–2439. https://doi.org/10.1175/1520-0493(1999)127<2419:TCKSRF>2.0.CO;2

Lee, W.-C., & Marks, F. D. Jr. (2000). Tropical cyclone kinematic structure retrieved from single-Doppler radar observations. Part II: The GBVTD-simplex center finding algorithm. *Monthly Weather Review*, *128*(6), 1925–1936. https://doi.org/10.1175/1520-0493(2000)128<1925:TCKSRF>2.0.CO;2

Lorsolo, S., Schroeder, J. L., Dodge, P., & Marks, F. (2008). An observational study of hurricane boundary layer small-scale coherent structures. *Monthly Weather Review*, *136*(8), 2871–2893. https://doi.org/10.1175/2008MWR2273.1

Marks, F. D., & Houze, R. A. (1987). Inner core structure of Hurricane Alicia from airborne Doppler radar observations. *Journal of the Atmospheric Sciences*, *44*(9), 1296–1317. https://doi.org/10.1175/1520-0469(1987)044<1296:ICSOHA>2.0.CO;2

Montgomery, M. T., & Kallenbach, R. J. (1997). A theory for vortex Rossby-waves and its application to spiral bands and intensity changes in hurricanes. *Quarterly Journal of the Royal Meteorological Society*, *123*(538), 435–465. https://doi.org/10.1002/qj.49712353810

National Oceanic and Atmospheric Administration, O. for C. M. (2018). National Land Cover Database. Retrieved August 20, 2006, From www.coast.noaa.gov/ccapftp

Oye, R. C., Mueller, C., & Smith, S. (1995). Software for radar translation, visualization, editing, and interpolation. In *27th Conference on Radar Meteorology* (pp. 359–361). Vail, CO: Amer. Meteor. Soc.

Potvin, C. K., Betten, D., Wicker, L. J., Elmore, K. L., & Biggerstaff, M. I. (2012). 3DVAR vs. traditional dual-Doppler wind retrievals of a simulated supercell thunderstorm. *Monthly Weather Review*, *140*(11), 3487–3494. https://doi.org/10.1175/MWR-D-12-00063.1

Powell, M. D. (1993). Wind measurement and Archival under the Automated Surface Observing System (ASOS): User concerns and opportunity for improvement. *Bulletin of the American Meteorological Society*, *74*(4), 615–623. https://doi.org/10.1175/1520-0477(1993)074<0615:WMAAUT>2.0.CO;2

Powell, M. D., & Houston, S. H. (1996). Hurricane Andrew's landfall in South Florida. Part II: Surface wind fields and potential real-time applications. *Weather and Forecasting*, *11*(3), 329–349. https://doi.org/10.1175/1520-0434(1996)011<0329:HALISF>2.0.CO;2

Powell, M. D., & Houston, S. H. (1998). Surface wind fields of 1995 Hurricanes Erin, Opal, Luis, Marilyn, and Roxanne at landfall. *Monthly Weather Review*, *126*(5), 1259–1273. https://doi.org/10.1175/1520-0493(1998)126<1259:SWFOHE>2.0.CO;2

Powell, M. D., Houston, S. H., & Reinhold, T. A. (1996). Hurricane Andrew's landfall in South Florida. Part I: Standardizing measurements for documentation of surface wind fields. *Weather and Forecasting*, *11*(3), 304–328. https://doi.org/10.1175/1520-0434(1996)011<0304:HALISF>2.0.CO;2

Powell, M. D., Vickery, P. J., & Reinhold, T. A. (2003). Reduced drag coefficient for high wind speeds in tropical cyclones. *Nature*, *422*(6929), 279–283. https://doi.org/10.1038/nature01481

Rappaport, E. N. (2014). Fatalities in the United States from Atlantic tropical cyclones: New data and interpretation. *Bulletin of the American Meteorological Society*, *95*(3), 341–346. https://doi.org/10.1175/BAMS-D-12-00074.1

Reasor, P. D., Montgomery, M. T., Marks, F. D., & Gamache, J. F. (2000). Low-wavenumber structure and evolution of the hurricane inner core observed by airborne dual-Doppler radar. *Monthly Weather Review*, *128*(6), 1653–1680. https://doi.org/10.1175/1520-0493(2000)128<1653:LWSAEO>2.0.CO;2

Rogers, R. F., Aberson, S., Bell, M. M., Cecil, D. J., Doyle, J. D., Kimberlain, T. B., Morgerman, J., et al. (2017). Rewriting the tropical record books: The extraordinary intensification of Hurricane Patricia (2015). *Bulletin of the American Meteorological Society*, *98*(10), 2091–2112. https://doi.org/10.1175/BAMS-D-16-0039.1

Sibson, R. (1981). A brief description of natual neighbor interpolation. In *Interpreting multivariate data* (pp. 21–36). New York: John Wiley & Sons.

Smith, R. K., & Montgomery, M. T. (2014). On the existence of the logarithmic surface layer in the inner core of hurricanes. *Quarterly Journal of the Royal Meteorological Society*, *140*(678), 72–81. https://doi.org/10.1002/qj.2121

Sparks, P. R., Schiff, S. D., & Reinhold, T. A. (1994). Wind damage to envelopes of houses and consequent insurance losses. *Journal of Wind Engineering and Industrial Aerodynamics*, *53*(1–2), 145–155. https://doi.org/10.1016/0167-6105(94)90023-X

Stern, D. P., Bryan, G. H., & Aberson, S. D. (2016). Extreme low-level updrafts and wind speeds measured by dropsondes in tropical cyclones. *Monthly Weather Review*, *144*(6), 2177–2204. https://doi.org/10.1175/MWR-D-15-0313.1

Wakimoto, R. M., Murphey, H. V., Dowell, D. C., & Bluestein, H. B. (2003). The Kellerville tornado during VORTEX: Damage survey and Doppler radar analyses. *Monthly Weather Review*, *131*(10), 2197–2221. https://doi.org/10.1175/1520-0493(2003)131<2197:TKTDVD>2.0.CO;2

Wakimoto, R. M., & Srivastava, R. (2017). Radar and atmospheric science: A collection of essays in honor of David Atlas. *Bulletin of the American Meteorological Society*, *98*(8), 1697–1715. https://doi.org/10.1175/BAMS-D-15-00130.1

Wang, Y. (2002a). Vortex Rossby waves in a numerically simulated tropical cyclone. Part I: Overall structure, potential vorticity, and kinetic energy budgets. *Journal of the Atmospheric Sciences*, *59*(7), 1213–1238. https://doi.org/10.1175/1520-0469(2002)059<1213:VRWIAN>2.0.CO;2

Wang, Y. (2002b). Vortex Rossby waves in a numerically simulated tropical cyclone. Part II: The role in tropical cyclone structure and intensity changes. *Journal of the Atmospheric Sciences*, *59*, 1239–1262. https://doi.org/10.1175/1520-0469(2002)059<1239:VRWIAN>2.0.CO;2

Weiss, C. C., & Schroeder, J. L. (2008). StickNet: A new portable rapidly deployable surface observation system. *Bulletin of the American Meteorological Society*, *89*(10), 1469–1506. https://doi.org/10.1175/1520-0477-89.10.1469.

Wingo, S. M., & Knupp, K. R. (2016). Kinematic structure of mesovortices in the eyewall of Hurricane Ike (2008) derived from ground-based dual-Doppler analysis. *Monthly Weather Review*, *144*(11), 4245–4263. https://doi.org/10.1175/MWR-D-16-0085.1

Wurman, J., & Kosiba, K. (2018). The role of small-scale vortices in enhancing surface winds and damage in Hurricane Harvey (2017). *Monthly Weather Review*, *146*(3), 713–722. https://doi.org/10.1175/MWR-D-17-0327.1